Atomistic absorption spectra and non-adiabatic dynamics of the LH2 complex with a GPU-accelerated *ab initio* exciton model

Aaron Sisto,[1,2] Clem Stross,[3] Marc van der Kamp,[3,4] Michael O'Connor,[3,5]
Simon McIntosh-Smith,[3] Graham T. Johnson,[6,7] Edward G. Hohenstein,[8] Fred R. Manby,[3]
David R. Glowacki,*[3,5] Todd J. Martinez*[1,2]

[1]*PULSE Institute and Department of Chemistry, Stanford University, Stanford, CA 94305, USA*
[2]*SLAC National Accelerator Laboratory, Menlo Park, California 94025, USA*
[3]*School of Chemistry, University of Bristol, Bristol, BS8 1TS, UK*
[4]*School of Biochemistry, University of Bristol, Bristol, BS8 1TD, UK*
[5]*Department of Computer Science, University of Bristol, BS8 1UB, UK*
[6]*California Institute for Quantitative Biosciences (QB3), University of California, San Francisco, CA 94158, USA*
[7]*Department of Bioengineering and Therapeutic Sciences, University of California, San Francisco, CA 94158, USA*
[8]*Department of Chemistry and Biochemistry, City College of New York, New York, NY 10031, USA*

Abstract

Recently, we outlined an efficient multi-tiered parallel excitonic framework that utilizes time dependent density functional theory (TDDFT) to calculate ground/excited state energies and gradients of large supramolecular complexes in atomistic detail. In this article, we apply our *ab initio* exciton framework to the 27 coupled bacteriocholorophyll-a chromophores which make up the LH2 complex, using it to compute: (1) linear absorption spectra; and (2) short-time, on-the-fly nonadiabatic surface-hopping (SH) dynamics of electronically excited LH2. In part one of this article, we refine our *ab initio* exciton model through the inclusion of two key parameters whose values are determined by fitting to experiment: a shift δ, which added to the diagonal elements corrects for the error in TDDFT vertical excitation energies on a single chromophore; and an effective dielectric constant ε, which applied to the off-diagonal matrix elements describes the average screening of the inter-chromophore transition-dipole coupling. Using snapshots obtained from equilibrium molecular dynamics simulations (MD) of LH2, we obtain values of both δ and ε through fitting to the thermally broadened experimental absorption spectrum, giving a linear absorption spectrum that agrees reasonably well with experiment. In the part two of this article, we construct a time-resolved picture of excitation energy transfer (EET) dynamics in the sub-picosecond regime following photoexcitation. Assuming Franck-Condon excitation of a narrow eigenstate band centred at 800 nm, we use surface hopping to follow a single nonadiabatic dynamics trajectory within the full eigenstate manifold. Consistent with experimental data, this trajectory gives timescales for $\mathrm{B800} \rightarrow \mathrm{B850}$ population transfer ($\tau_{B800 \rightarrow B850}$) between 650 – 1050 fs, and B800 population decay ($\tau_{800 \rightarrow}$) between 10 – 50 fs. The dynamical picture that emerges is one of rapidly fluctuating LH2 eigenstates that are delocalized over multiple chromophores and undergo frequent crossing on a femtosecond timescale as a result of the atomic vibrations of the constituent chromophores. The eigenstate fluctuations arise from disorder in both the diagonal chromophore site energies and the off-diagonal inter-chromophore couplings. The scalability of our *ab initio* excitonic computational framework across massively parallel architectures opens up the possibility of addressing a wide range of questions, including how specific dynamical motions impact both the pathways and efficiency of electronic energy-transfer within large supramolecular systems.

* drglowacki@gmail.com; toddjmartinez@gmail.com

1 Introduction

Photosynthetic systems efficiently transfer the energy absorbed from incident solar radiation from light harvesting "antenna" complexes to photosynthetic reaction centres. Numerous studies have shown that this energy transport is of near unit efficiency across distances of hundreds of nanometers.[1-4] From the perspective of both time-independent and time-dependent spectroscopy, probably the most well-studied photosynthetic system is the light harvesting II (LH2) complex found in purple bacteria,[5-12] schematically depicted in Figure 1. Explicit atomistic simulation of non-adiabatic dynamics in photosynthetic light-harvesting complexes presents a significant challenge owing to their size. For example, LH2 (Figure 1) contains 27 constituent bacteriochlorophyll-a chromophores (Bchla) (each with over a hundred atoms).[13] This is in addition to the protein environment and a set of embedded carotenoids. As a result, most modelling studies adopt course-grained approaches that average over the details of the atomistic dynamics – e.g., in the form of course-grained perturbative and Markovian master equations.[14-18] Alternative approaches use atomistic insight from first principles calculations to directly propagate approximate equations of motion for the electrons and nuclei.[19] For example, one of the most common course-grained strategies for modelling light harvesting dynamics utilizes the hierarchical equations of motion (HEOM), which is applicable to any process occurring within a system characterized by N discrete quantum states coupled to a bosonic environment (which can be an infinite collection of harmonic oscillators characterized by some spectral density).[20, 21] The HEOM and related approaches have been utilized by a number of workers to describe population transfer in photosynthetic light harvesting systems.[22-24]

A wide range of methods has been previously employed to obtain parameters for coarse-grained exciton Hamiltonians. At one extreme are entirely empirical models, with Hamiltonian parameters obtained through fitting to experimental observables like absorption spectra.[25] However, there have also been efforts toward developing hybrid approaches, where coarse-grained model parameters are obtained from atomistic simulations.[26] The general strategy here has been to carry out atomistic molecular dynamics (MD) to sample a range of atomic configurations within the antenna complex. After extracting chromophore geometries from the MD simulations, *ab initio* methods have been used to calculate ground and excited-state chromophore site energies and couplings.[17, 19, 27, 28] Although these approaches include some atomistic detail in the dynamical propagation, they nevertheless average over many of the constituent atomic motions of both the environment and the

system. The quantum system is collapsed onto a set of site energies, the environment is collapsed into a spectral density function, and the system-environment coupling is collapsed into a set of linear functional forms. Such coarse-grained models are certainly useful insofar as they enable comparison with phenomenological observables obtained from experiment. However, an important fundamental issue that has recently arisen in understanding light harvesting systems concerns the extent to which electronic energy transport and delocalized electronic excitations are coupled to vibrational motion.[29-35] Because coarse-graining largely averages over the impact that specific, local vibrational motions have on excitation energy transfer (EET) dynamics, the work presented here marks an important step toward developing fully atomistic non-adiabatic MD simulations of condensed phase light harvesting systems which will ultimately provide a detailed understanding of the relationship between specific atomic motions and phenomenological EET dynamics. This is an outstanding area of interest within the domain of biological light harvesting specifically, and photo-excited energy transport more generally.[36-38]

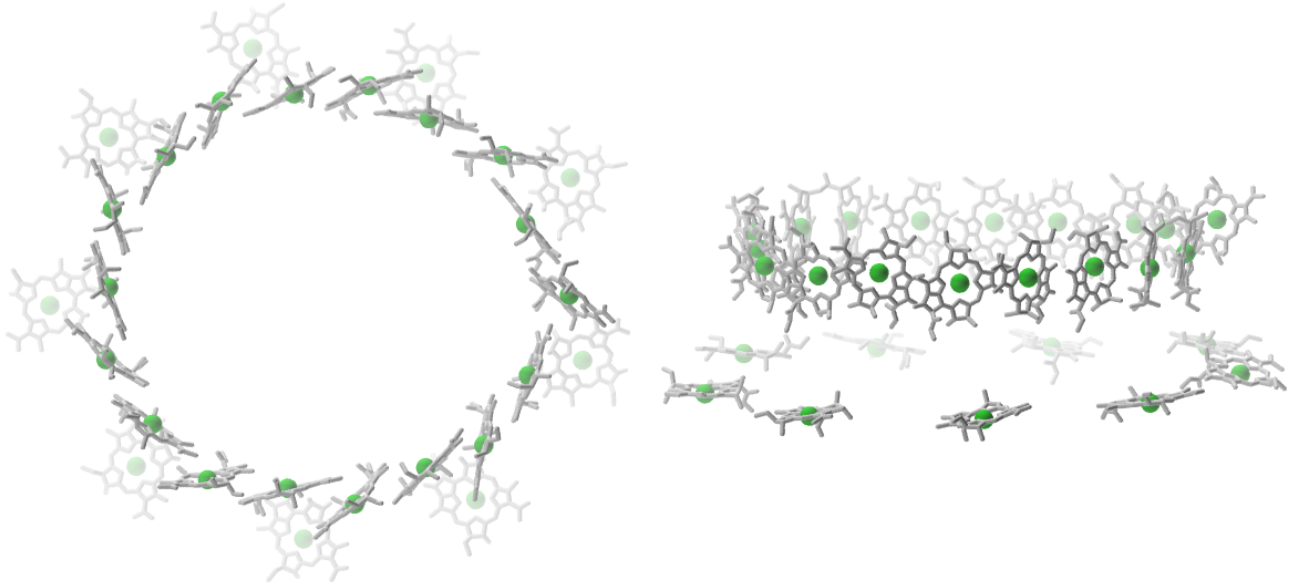

Figure 1: The 27 Bchla chromophores comprising LH2, from 'top-down' (left panel) and 'side-on' (right panel) views. LH2 consists of two different ring structures: a 9-chromophore B800 ring (named for its spectral absorption maximum at 800 nm), and an 18-chromophore B850 ring (named for its absorption maximum at 850 nm). The 18 chromophores of the B850 ring form 9 adjacent dimer pairs. The phytyl tails of the BChlas, along with the surrounding protein scaffold and carotenoids, have been removed for the sake of clarity.

For small molecular systems, excited state methods like CASSCF, CASPT2, EOM-CCSD, and TDDFT can provide considerable insight into specific atomic motions and molecular vibrations which correlate with dynamical phenomena like intersystem crossing and internal conversion, especially in combination with algorithms designed for atomistic non-adiabatic dynamics simulations.[39-44] With increasing research effort devoted to investigating condensed phase electronic

energy transfer across a range of systems,[2, 27, 40, 45-47] an open question is whether excited-state theoretical methods can be extended to large systems to furnish a similar level of detail, and thereby provide microscopic insight regarding the details of electronic energy transfer. TDDFT methods and their extensions[48] have recently shown some success in calculating the site energies of pigments in light harvesting complexes,[49, 50] and there have been recent attempts to carry out *ab initio* calculations on both the ground and excited states of these large supramolecular complexes.[51] In this work, we describe a new attempt to push atomistic dynamics simulation of light harvesting antenna complexes further. Utilizing a recently developed multi-tiered parallel exciton framework that has been shown to give good agreement with fully atomistic GPU-accelerated TDDFT methods,[52] we build an excitonic LH2 Hamiltonian which is refined through fitting two parameters to the experimental absorption spectrum. Using this fully atomistic Hamiltonian, we carry out some preliminary 'on-the-fly' non-adiabatic dynamics trajectories of the LH2 complex using Tully's fewest switches surface hopping (FSSH) algorithm.[53] Assuming Franck-Condon excitation of a narrow eigenstate band centred at 800 nm, we use surface hopping to follow the subsequent nonadiabatic dynamics within the full LH2 eigenstate manifold. Consistent with experimental data, our non-adiabatic dynamics simulations give respective timescales for $\mathrm{B800} \rightarrow \mathrm{B850}$ population transfer ($\tau_{B800 \rightarrow B850}$) between 650 – 1050 fs, and B800 population decay ($\tau_{800 \rightarrow}$) between 10 – 50 fs. To the best of our knowledge, these are amongst the first on-the-fly simulations of their kind performed on a photosynthetic supramolecular multi-chromophore complex of this size, and provide an intriguing way forward for future studies of energy transport in light harvesting systems.

2 Theoretical Framework

2.1 Atomistic Ab Initio Exciton Model

The TDDFT excitonic framework used in this work has been described previously.[52] Therefore, we provide only a brief summary here, with some additional information available in the SI. We define the many electron basis set $\Phi_{(i,k)}$ to include the singly-excited excitonic basis functions of the full system, with the *i*th chromophore excited to its *k*th electronic state and the other $N-1$ chromophores in their ground electronic state:

$$\Phi_{(i,k)} = \hat{A}\left(\varphi_{(1,0)}\varphi_{(2,0)}\cdots\varphi_{(i,k)}\cdots\varphi_{(N,0)}\right) \tag{3}$$

Here, it is assumed that the exciton basis functions described by the wavefunctions of the ground and singly-excited chromophores can be written as a single Slater determinant, where $\left|\varphi_{(i,k)}\right\rangle$ denotes the

Slater determinant describing the k^{th} electronic state wavefunction in the basis of molecular orbitals localized on the i^{th} chromophore. The ground electronic state, where none of the chromophores are excited, is also included in the many-electron basis.

Given this many-electron basis set, the exciton Hamiltonian is given as (N = 27 in the example below, corresponding to the constituent BChlas in Figure 1):

$$\mathbf{H} = \begin{bmatrix} E_0 & V_{(0)(1,1)} & \cdots & V_{(0)(N,1)} \\ V_{(0)(1,1)} & E_{(1,1)} & \cdots & V_{(1,1)(N,1)} \\ \vdots & \vdots & \ddots & \vdots \\ V_{(0)(N,1)} & V_{(1,1)(N,1)} & \cdots & E_{(N,1)} \end{bmatrix} \tag{1}$$

The first diagonal matrix element describes the energy of the exciton basis function for the ground state of the full system, $|\Phi_0\rangle$. The ground state energy, E_0, which does not typically appear in standard exciton models, allows us to describe both the ground-excited state electronic coupling and the ground and excited state gradients of the full system. The energy is evaluated as the sum of individual ground state chromophore energies coupled by a Coulombic dipole-dipole interaction, valid for well-separated chromophore geometries:[54]

$$E_0 = \sum_i \varepsilon_{(i,0)} + \frac{1}{\varepsilon_r} \sum_{j>i} \frac{\vec{\mu}_{(i,0)} \cdot \vec{\mu}_{(j,0)} - 3\left(\vec{n}_{ij} \cdot \vec{\mu}_{(i,0)}\right)\left(\vec{n}_{ij} \cdot \vec{\mu}_{(j,0)}\right)}{R_{ij}^3} \tag{2}$$

where ε_r is an effective dielectric constant, $\vec{n}_{ij}$ is the unit vector for the center-of-mass separation between chromophores i and j and $\varepsilon_{(i,0)} / \vec{\mu}_{(i,0)}$ are the ground state energy/dipole moment of the i^{th} chromophore, respectively.

The remaining diagonal elements describe the energies of the singly-excited excitonic basis functions:[52]

$$\begin{aligned} E_{(i,k)} = & \sum_{j \neq i} \varepsilon_{(j,0)} + \left(\varepsilon_{(i,k)} + \delta\right) + \\ & \frac{1}{\varepsilon_r} \sum_{j \neq i} \frac{\vec{\mu}_{(j,0)} \cdot \vec{\mu}_{(i,k)} - 3\left(\vec{n}_{ij} \cdot \vec{\mu}_{(j,0)}\right)\left(\vec{n}_{ij} \cdot \vec{\mu}_{(i,k)}\right)}{R_{ij}^3} + \\ & \frac{1}{\varepsilon_r} \sum_{m>n;m,n \neq i} \frac{\vec{\mu}_{(m,0)} \cdot \vec{\mu}_{(n,0)} - 3\left(\vec{n}_{mn} \cdot \vec{\mu}_{(m,0)}\right)\left(\vec{n}_{mn} \cdot \vec{\mu}_{(n,0)}\right)}{R_{mn}^3} \end{aligned} \tag{4}$$

where $\varepsilon_{(i,k)}$ is the energy of the k^{th} excited state of the i^{th} chromophore, $\varepsilon_{(j,0)}$ is the ground state energy of the j^{th} chromophore, and $\vec{\mu}_{(i,k)}$ is the dipole moment of the k^{th} excited state on chromophore i. The correction factor δ is an energy shift parameter that accounts for the inevitable discrepancies between experimental excitation energies and those calculated from TDDFT.[55] The off-diagonal matrix elements describe the Coulombic coupling between excitonic basis states and are approximated using the Forster expression,[56] within the point-dipole approximation:

$$V_{(i,k)(j,l)} = \left\langle \mathbf{\Phi}_{(i,k)} \middle| \hat{H} \middle| \mathbf{\Phi}_{(j,l)} \right\rangle \approx \frac{1}{\varepsilon_r} \frac{\vec{M}_{(i,k)\leftarrow(i,0)} \bullet \vec{M}_{(j,l)\leftarrow(j,0)} - 3\left(\vec{n}_{ij} \bullet \vec{M}_{(i,k)\leftarrow(i,0)}\right)\left(\vec{n}_{ij} \bullet \vec{M}_{(j,l)\leftarrow(j,0)}\right)}{R_{ij}^3} \tag{5}$$

where $\vec{M}_{(i,k)\leftarrow(i,0)}$ is the transition dipole moment for transition $k\leftarrow0$ on chromophore i. The off-diagonal matrix elements that couple the ground state to excited chromophore states are calculated as:

$$V_{(0)(j,l)} = \left\langle \mathbf{\Phi}_0 \middle| \hat{H} \middle| \mathbf{\Phi}_{(j,l)} \right\rangle \approx \frac{1}{\varepsilon_r} \frac{\vec{\mu}_{(i,0)} \bullet \overrightarrow{M}_{(j,l)} - 3\left(\vec{n}_{ij} \bullet \vec{\mu}_{(i,0)}\right)\left(\vec{n}_{ij} \bullet \overrightarrow{M}_{(j,l)}\right)}{R_{ij}^3} \tag{6}$$

The point dipole interactions fall off as $1/\varepsilon_r R_{ij}^3$, where R_{ij} is the separation distance between chromophores i and j, and ε_r is the effective dielectric constant. The effective dielectric constant describes the extent to which the coupling is electrostatically screened by the local environment. The model defined by Eqs. (2) and (4-6) is most accurate in the limit of large R, where higher order multipole terms are insignificant relative to the leading-order dipole-dipole interaction terms and the exponential decay of the neglected Dexter-type terms renders them negligible.[57]

Within this excitonic framework, the electronic absorption spectrum $I(\omega)$ can be computed over a range of conformational samples (each of which is indexed by α) using the following expression:

$$I(\omega) = \sum_{I,\alpha} f_{I,\alpha} \frac{1}{\mathbf{\Gamma}\sqrt{2\pi}} \exp\left(\frac{-\left(\mathbf{\Omega}_{I,\alpha} - \omega\right)^2}{\mathbf{\Gamma}^2} \right) \tag{7}$$

where $f_{I,\alpha}$ is the calculated oscillator strength for transition from the lowest excitonic eigenstate ψ_0 to ψ_I at snapshot α (described previously[52]), $\Omega_{I,\alpha}$ is the corresponding excitation energy, and Γ is a

Gaussian broadening factor. The excitonic eigenstates ψ are obtained by diagonalization of the Hamiltonian in Eq. (1).

It is important to point out that more accurate expressions for the inter-chromophore transition-dipole couplings are available than those afforded by the point-dipole model utilized here.[58-64] These expressions include the transition density cube method,[59] the transition monopole approximation,[60, 61] the transition charge method,[58] and others.[62-64] Our decision to adopt the point-dipole approximation stems from a few different considerations. First, the point-dipole model is straightforward to differentiate compared to the other strategies, which is an important consideration given that one of our primary aims is to follow non-adiabatic dynamics on the excitonic eigenstates. Second, previous work has shown that the point-dipole approximation is quite accurate for the transition dipole coupling strength between Bchla chromophores in LH2.[58, 65, 66] Our own work is indeed compatible with this last observation:[52] an excitonic model built from point-dipole couplings between the chromophore transition dipoles gives eigenstate energies and linear absorption spectra which are in very good agreement with the results obtained from GPU-accelerated TDDFT calculations on a six-chromophore subset of adjacent LH2 BChlas. Recently, a variant of an *ab initio* exciton model that analytically calculates the Coulombic and Dexter-type exchange couplings has been introduced.[67, 68] This demonstrates that higher accuracy can be achieved if desired, although the computational cost is also much increased.

2.2 Parameter Optimization

Diagonalizing the Hamiltonian in Eq. (1) yields N+1 adiabatic eigenvalues λ_i and eigenvectors ψ_i in the exciton basis (the ground electronic state and N excited states). Agreement between the linear absorption spectrum obtained using these eigenstates and the experimental spectrum is sensitive to the δ and ε_r parameters in Eqs. (3-5). In this work, δ and ε_r have been determined by fitting to the experimental linear absorption spectrum using a non-linear least squares approach borrowed from previous work.[69] The decision to optimize the δ and ε_r parameters arises from the recognition that: (i) TDDFT vertical excitation energies are usually subject to some systematic error; and (ii) the dielectric screening in Eqs. (4-5) is an underestimate of the true screening, because the coupling between BChlas includes neither the explicit effects of the environment nor of the other BChlas beyond the Forster coupling described above.

2.3 Nonadiabatic exciton dynamics

The results of our fitting procedure (discussed below) provide reasonable eigenstate energies, but non-adiabatic dynamics methods also require efficient ground and excited-state gradients and

non-adiabatic coupling vectors between all excitonic eigenstates. For example, the non-adiabatic coupling vectors, $\vec{d}_{IJ}$, which mediate population transfer between excitonic states, are evaluated as:

$$\vec{d}_{IJ} = \frac{\partial \mathbf{H}_{IJ} / \partial R}{\lambda_J - \lambda_I} \tag{8}$$

where $d\mathbf{H}/dR$ (in the adiabatic representation) can be calculated from the Hellmann-Feynmann theorem, the excitonic eigenstates and the gradients of the matrix elements in Eq. (1). Derivatives of the diagonal elements of the Hamiltonian in Eq. (1) (for the exciton basis states $\mathbf{\Phi}_{(i,k)}$) may be written as:

$$\begin{aligned}
&\frac{\partial E_{(i,k)}}{\partial R} = \frac{\partial \varepsilon_{(i,k)}}{\partial R} + \sum_{j \neq i} \frac{\partial \varepsilon_{(j,0)}}{\partial R} + \\
&\frac{1}{\varepsilon_r} \sum_{j \neq i} \frac{\partial}{\partial R} \left[\frac{\vec{\mu}_{(j,0)} \cdot \vec{\mu}_{(i,k)} - 3\left(\vec{n}_{ij} \cdot \vec{\mu}_{(j,0)}\right)\left(\vec{n}_{ij} \cdot \vec{\mu}_{(i,k)}\right)}{R_{ij}^3} \right] + \\
&\frac{1}{\varepsilon_r} \sum_{j>l, j,l \neq i} \frac{\partial}{\partial R} \left[\frac{\vec{\mu}_{(j,0)} \cdot \vec{\mu}_{(l,0)} - 3\left(\vec{n}_{ij} \cdot \vec{\mu}_{(j,0)}\right)\left(\vec{n}_{ij} \cdot \vec{\mu}_{(l,0)}\right)}{R_{ij}^3} \right]
\end{aligned} \tag{9}$$

The derivatives of the corresponding off-diagonal elements are given by the analytical derivatives of matrix elements in Eqs. (4-5). (See section S1 of the Supplementary Information for the full gradient expressions).

Ground and excited state gradients of individual chromophores are readily computed from TDDFT, allowing efficient evaluation of the $\partial\varepsilon/\partial R$ terms in Eq. (8). Obtaining derivatives for the transition dipole moments, $\partial \boldsymbol{M}/\partial R$, and excited state dipole moments, $\partial \boldsymbol{\mu}_{(i,k)}/\partial R$, is significantly more challenging, because it requires solving higher order coupled-perturbed equations. Tractable non-adiabatic gradients within the exciton Hamiltonian are requisite for MD simulations on systems as large as LH2, with the principle bottleneck being the ability to efficiently calculate analytic gradients of the chromophore transition dipole moments. To avoid this expense in the context of the surface hopping MD simulations of LH2, we used a simple approximation to the excited state and transition dipole derivatives: assuming a ground and excited state charge distribution which is only slowly varying with respect to nuclear conformation, we took the atomic-specific Cartesian values of $\partial\mathbf{M}/\partial$R and $\partial \boldsymbol{\mu}_{(i,k)}/\partial R$ to be static quantities, obtained as the average values of numerically

differentiated dipole vectors for the $S_0 \rightarrow S_1$ excitation or S_1 excited state on a particular Bchla chromophore.

The averaged values of $\partial \mathbf{M}/\partial R$ which we used to carry out the surface hopping dynamics are described in part 2 of the Supplementary Information, and were calculated numerically by finite difference (with displacements of 0.001 Angstrom) averaged over 100 conformational snapshots sampled from MD simulations of LH2 carried out in AMBER (described below). The distribution of atoms which contribute significantly to the magnitude of the derivative vector include only the heavy atoms in the core and inner rings, indicating that it is in fact the orientation of these inner atoms with respect to the Mg core that plays a dominant role in the fluctuations of the transition dipole vectors on each B850 site. In our previous work, we have carried out a comparison of the dynamics results obtained using this approximation to those obtained using numerical transition dipole moments calculated from full TDDFT, and shown that both approaches are in close agreement.[52] Part S2 of the Supplementary Information details results from two additional tests (carried out on six- and two-chromophore LH2 subsets, respectively) which were designed to test our static approximation: (1) a comparison between the transition dipole moment gradient vector obtained using the static approximation with the same quantity obtained using TDDFT simulations; and (2) a comparison between a 100-fs MD run obtained using our static approximation with a 100-fs MD run obtained using analytical dipole derivatives calculated using the Lagrangian approach described previously.[70] In both cases, the tests indicate very good agreement. Figure S1 further supports the approximation that the transition dipole moment derivatives are only weakly dependent on variations of the Bchla atomic coordinates.

2.4 Surface Hopping Dynamics

Using the approach described above, we ran dynamics of the full 27-chromophore LH2 complex, using the fewest-switches surface hopping algorithm,[53] in which the electronic wave function is expressed as an expansion of adiabatic excitonic eigenstates:

$$\mathbf{\Psi}\left(r,R,t\right)=\sum_{I=0}^{N}c_I(t)\psi_I\left(r,R,t\right) \tag{10}$$

where c_I are the time-dependent, complex expansion coefficients and ψ_I are the wavefunctions of the excitonic eigenstates. At each dynamics timestep, the exciton Hamiltonian is diagonalized and gradients and nonadiabatic coupling vectors are obtained. The coefficients are then propagated via the time-dependent Schrodinger Equation:

$$i\hbar\dot{c}_k = \sum_j c_j \left(V_{kj} - i\hbar \dot{\vec{R}} \cdot \vec{d}_{kj} \right) \tag{11}$$

where $\dot{\vec{R}}$ is a vector of the classical nuclear velocities of a trajectory propagated on a particular Born-Oppenheimer PES, which enters Eq. (10) through a dot product with the non-adiabatic coupling vectors defined in Eq. (8). The off-diagonal matrix element V_{kj} vanishes in the adiabatic representation, i.e., $V_{kj} = \varepsilon_k \delta_{kj}$. The fewest switches surface-hopping algorithm has some well-known problems related to electronic coherence.[71-73] These can be avoided by using multiple spawning dynamics,[74-76] but we leave such studies to future work. For this work, our choice of the surface-hopping algorithm is largely driven by computational cost – surface hopping requires only a single excited state gradient per timestep.

The initial excitation pulse in the surface hopping simulations assumed a Gaussian profile centered at ε_I in energy, with an empirical full width half max (FWHM). The excitation probability and initial population for each electronic eigenstate I is computed as the product of the Gaussian pulse profile, $\phi_G(\varepsilon_I)$, at the energy of the electronic eigenstate, ε_I, multiplied by the oscillator strength of the electronic eigenstate, f_I:

$$p_I = N\phi_G(\varepsilon_I) f_I \tag{12}$$

where N is the normalization factor. Observable quantities are computed from a single initial condition with initial population amplitudes specified by Eq. (12). In practice, Eq. (12) places the bulk of the initial amplitude on a single excitonic eigenstate.

3 Computational Methods

3.1 GPU-accelerated TDDFT

Calculations of the ground state electronic structure for each Bchl chromophore used the 6-31G basis set and the ωPBEh exchange correlation functional with range separation parameter ω=0.2 Å^{-1}. Energies, gradients, and dipole moments for the lowest excited state of each chromophore were calculated using linear response TDDFT (LR-TDDFT) within the Tamm-Dancoff approximation.[77] The SCF and TDDFT calculations for each BChla chromophore are carried out with GPU-accelerated algorithms, as implemented in TeraChem.[52] Since the calculations for each Bchla are independent of all other Bchla chromophores, we employ independent compute nodes for each chromophore and calculate these in parallel.[52] The excitonic framework outlined above is implemented within a self-contained software package which utilizes a Python implementation of the message passing interface (MPI) similar to that recently described.[78] The MPI framework distributes

individual Bchla TDDFT jobs on hybrid CPU/GPU nodes, retrieving the appropriate results at the conclusion of the job (i.e., ground and excited-state energies and gradients of a specific Bchla chromophore), and then reducing this data to form the exciton Hamiltonian on the master CPU node, which undertakes diagonalization to obtain the eigenstate coefficients, eigenvalue energies, and state-specific atomic gradients required for dynamical propagation. The excitonic Hamiltonians required to propagate the surface hopping trajectory described below were run in parallel on 16 GTX 750 Ti GPUs distributed across 2 compute nodes (8 GPUs each), with the ERIs of an individual chromophore parallelized over 4 GPUs.

3.2 LH2 Thermal MD simulations

For the purposes of exciton spectral fitting and in order to generate initial geometries for surface-hopping dynamics simulations, MD simulations of the LH2 complex were carried out, with the Bchla chromophores and carotenoids explicitly embedded in the LH2 protein environment. Atomistic thermal LH2 MD simulations were performed on GPUs with the pmemd.cuda code[79] that is part of the AMBER12 suite of programs (www.ambermd.org). PDB-entry 2FKW[80] was used as starting structure, with the lauryl dimethylamine-N-oxide (LDA) molecules removed. The ff12SB force-field was used for the protein components and bacteriochlorophylls were modelled using the parameters from Ceccarelli, et al.[81] Parameters for the N-terminal N-carboxymethionine of the peptide chains were adapted from the ff12SB parameters for standard methionine. For the rhodopsin glucoside (RG1) carotenoids, we combined parameters from Zhang et al.[82] (for the rhodopsin part, based on β-carotene) and GLYCAM06 (for the glucoside part).[83] AM1-BCC charges[84] (calculated through Antechamber) were used for the rhodopsin part and the link to the glucoside. The system was set up for simulation using the generalized Born implicit solvent method (model II in ref. [85]). Histidines were singly protonated on Nε2, apart from His30/His31 that coordinate to the magnesium in bacteriochlorophyll through Nε2 (and were thus protonated on Nδ1). Simulations were performed in the NVT ensemble, using 298K Langevin dynamics for temperature control and a 2 fs time step (with SHAKE applied to hydrogen containing bonds). No cut-off for non-bonded interactions was used, and calculations were performed with the Mixed Single/Double/Fixed Point Precision CUDA code. After a short minimization, the system was gradually heated and equilibrated at 300 K over 200 ps, before starting production MD in 1 ns time-blocks. For production MD, a mild restraint was applied (force constant of 10 kcal mol^{-1} $Å^{-2}$) when the Nε2-Mg distance was larger than 3.0 Å. The ESI shows a movie of the 300 K AMBER MD simulations (see file AMBER-MD.mov).

3.3 Parameter Fitting and Surface Hopping

Fitting of δ and ε_r was carried out by extracting 500 snapshots of Bchla conformations from the LH2 AMBER MD simulations (i.e., one snapshot every 100 fs) using a SciPy non-linear Levenberg-Marquardt algorithm we have described and utilized previously.[69, 78] With δ and ε_r as fitting parameters, we minimized a merit function defined as the sum-of-squares difference between the 293K experimental linear absorption spectrum and the excitonic 298K absorption spectrum:

$$\chi(\delta,\varepsilon_r) = \sum_{\omega} \left(I(\omega)^{exciton} - I(\omega)^{\text{experiment}} \right)^2 \tag{13}$$

where the summation is over the discretized excitation energy ω, and I(ω) is the corresponding absorption spectrum amplitude, as described previously.[52] The Gaussian broadening factor Γ which appears in Eq (7) was not varied during the fits. Instead, it remained a fixed parameter with a value of 10 meV – essentially the minimum required to give a smooth absorption spectrum for comparison to the experimental spectrum. Optimization runs where we varied Γ as well as δ and ε_r showed no substantial improvements in the fit, nor did they yield an appreciable change in the overall absorption lineshape, beyond a slight smoothing of local variations in the spectrum which arise as a consequence of conformational sampling.

The surface hopping dynamics relied on a Velocity-Verlet NVE algorithm for propagating nuclear coordinates with a time step of 0.2 fs, along with a 4th order Runge-Kutta algorithm to integrate the time-dependent Schrodinger Equation in the adiabatic exciton basis. Initial velocities for the surface-hopping trajectories were sampled from a 300K Boltzmann distribution, with initial positions selected from a randomly chosen single dynamics snapshot obtained from the LH2 MD simulations.

4 Results and Discussion

4.1 298K Absorption Spectra

The experimental absorption spectra[86] of LH2 from *Rhodopseudomonas acidophila* is shown in blue in Figure 2. The double-ring structure of LH2 shown in Figure 1 results in two prominent peaks separated by ~50 nm. The first peak amplitude is slightly greater than the highest peak, with a low energy band edge at ≈885 nm. Our fitting procedure yielded optimized values of -0.50 eV and 1.43 for the δ and ε_r parameters, respectively. Figure 2 shows the resultant spectra obtained from fitting, with absorption maxima at 865 and 800 nm. In order to further evaluate the agreement between the experimental and excitonic spectra, we examined the lineshapes of each absorption peak

by fitting a sum of two Gaussians to each spectrum using a nonlinear least squares algorithm with variable Gaussian amplitudes, means and standard deviations. The full-width half-max (FWHM) of the 800 and 850nm Gaussian linewidths exciton spectra are 57.23 nm and 33.27 nm, in close agreement with experimental values. Figure 2 shows a larger discrepancy between the experimental and the model predictions for the amplitude of the high-energy peak compared to the lower energy peak. The origins of this discrepancy are not entirely clear. Our initial hypothesis was that site-dependent screenings of the inter-chromophore couplings might be responsible. To probe this hypothesis, we introduced additional model parameters which effectively allowed us to vary the value of ε_r with respect to specific chromophore-chromophore couplings; however, this led to only negligible changes in the exciton spectrum and thus this hypothesis can be confidently excluded. Other possible reasons for the discrepancy in the peak height include errors in the TDDFT oscillator strengths or structural errors arising from the empirical force field.

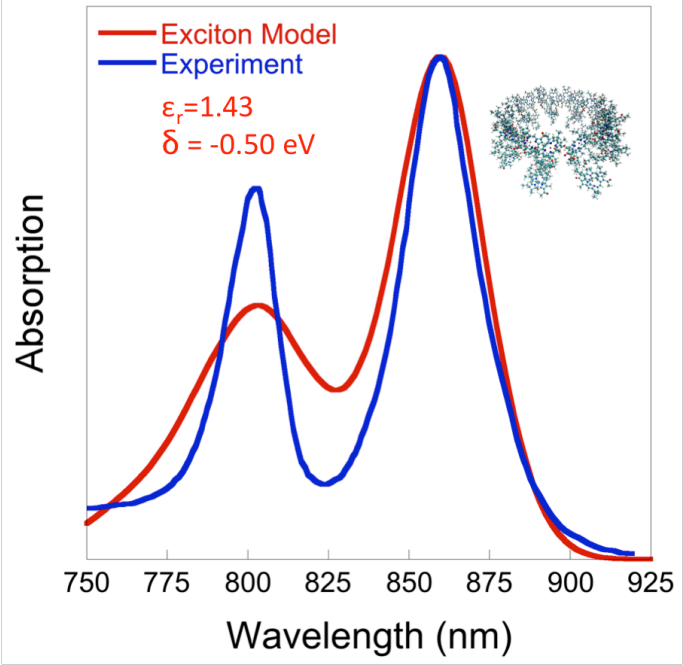

Figure 2: Absorption spectra of LH2 complex computed using exciton model (red) and from experiments (blue) carried out at 298K.[86] The best-fit parameters obtained from the exciton model are also shown.

Encouragingly, the best-fit parameters are in reasonable agreement with *a priori* expectations. Specifically, the best-fit value of δ (-0.50 eV), which red shifts the TDDFT vertical excitation energies, is compatible with the systematic errors often observed in TDDFT site energies. Red shifts linked to pigment-protein interactions are consistent with results observed in previous

studies,[51, 87, 88] and are as expected given that the vertical excitation energies on the chromophores are calculated *in vacuo*. The dielectric screening parameter ε_r accounts for the effect that the environment has in modulating the inter-chromophore coupling, effectively treating the gas-phase exciton model as if it were embedded in a homogeneous electrostatic environment. Our best-fit value of 1.43 is a relatively small correction, comparable to what might be expected in weakly interacting organic solvents. The primary effects of the dielectric screening value are to modulate the energetic gap between the two peaks shown in Figure 2, and to a lesser extent, the energetic bandwidths and peak intensities.

Obtaining an atomistic model that reproduces the experimental absorption spectrum, allows us to analyze the microscopic details of the electrostatic coupling between the different classes of LH2 chromophores. A key factor that impacts the structure of the experimental spectra is the distribution of exciton Hamiltonian matrix elements generated from thermally-induced LH2 conformations. The distribution of site energies corresponding to each exciton basis state reflects the variations in the S_1 excitation energy of each BChla chromophore. Our model gives a site energy distribution with an average of ~12625 cm^{-1} (Figure 3a), in agreement with previous estimates of the B850 S_1 excitation energy.[89] We have similarly analysed the distribution of interactions between BChlas in LH2. This includes interactions between all the BChlas, split into three different classes: interactions between BChlas on the B850 ring, interactions between BChlas on the B800 ring, and interactions between BChlas on the B800 ring with those on the B850 ring (Figure 3b). The distribution of intra-dimer B850-B850 Bchla couplings have an average value of 440 cm^{-1}. Inter-dimer couplings are markedly weaker, with an average of 125 cm^{-1} (Figure 3c). These results are broadly in line with previous estimates of intra- and inter-dimer B850 couplings, which generally lie between 238-771 cm^{-1} and 110-612 cm^{-1}, respectively.[89-93] The strong inter and intra-dimer coupling of the BChlas in the B850 ring arise from the short-range proximity of chromophores as well as the alignment of their transition dipole moment vectors within the ring structure. Figure 3d shows the coupling energies for B800-B850 interactions. The interactions between B800-B800 nearest neighbours and B800-B850 nearest neighbors have a similar distribution, with respective averages of 39 cm^{-1} and 46 cm^{-1}. These small values of the B800-B800 and B800-B850 couplings compared to the B850-B850 couplings are similar to the findings of previous work, which has estimated these couplings to be approximately 24 – 31 cm^{-1}.[5, 59] Long-range couplings are less than 10 cm^{-1}, for both distributions. The distributions of site energies and couplings in Figure 3 are essentially Gaussian, a finding which is qualitatively consistent with ideas put forth by Cheng and Silbey.[94] These authors

used a coarse-grained empirical exciton Hamiltonian to model exciton dynamics in the B800 ring of LH2 and examine the role that different types of disorder played in reproducing time-resolved spectroscopic results. They argued that representing both the chromophore site energies and the inter-chromophore couplings [i.e., the diagonal and the off-diagonal elements in Eq. (1)] as independent random Gaussian variables (which they called 'static disorder', and attributed to thermal structural fluctuations) was important to explaining both homogeneous and inhomogeneous lineshapes of the B800 band.

Our calculated absorption spectrum reproduces the experimental spectrum reasonably well. The ratio of the integrals under the B850 band (model:experiment) are effectively unity; for the B800 band the ratio is 0.92. The biggest discrepancy concerns the amplitude of the B800 band, which the model underpredicts compared to the experimental spectrum, and it is worth briefly highlighting potential reasons for this: (1) the MD simulations (from which our absorption spectra were calculated) were initialized from an LH2 crystal structure which is very close to a perfect circle and (even over the course of hundreds of nanoseconds) were unable to sample elliptical configurations which have previously been shown to play an important role in quantitatively modeling the experimental spectra;[95] (2) the absorption spectra which we calculated using the *ab initio* exciton model were carried out with all 27 chromophores in the gas phase, with no environment apart from neighboring chlorophylls. As a result, the site-specific excitation energies, transition dipoles, and oscillator strengths of the LH2 eigenstate transitions may not align exactly with their values given an explicit treatment of the environment electrostatics.

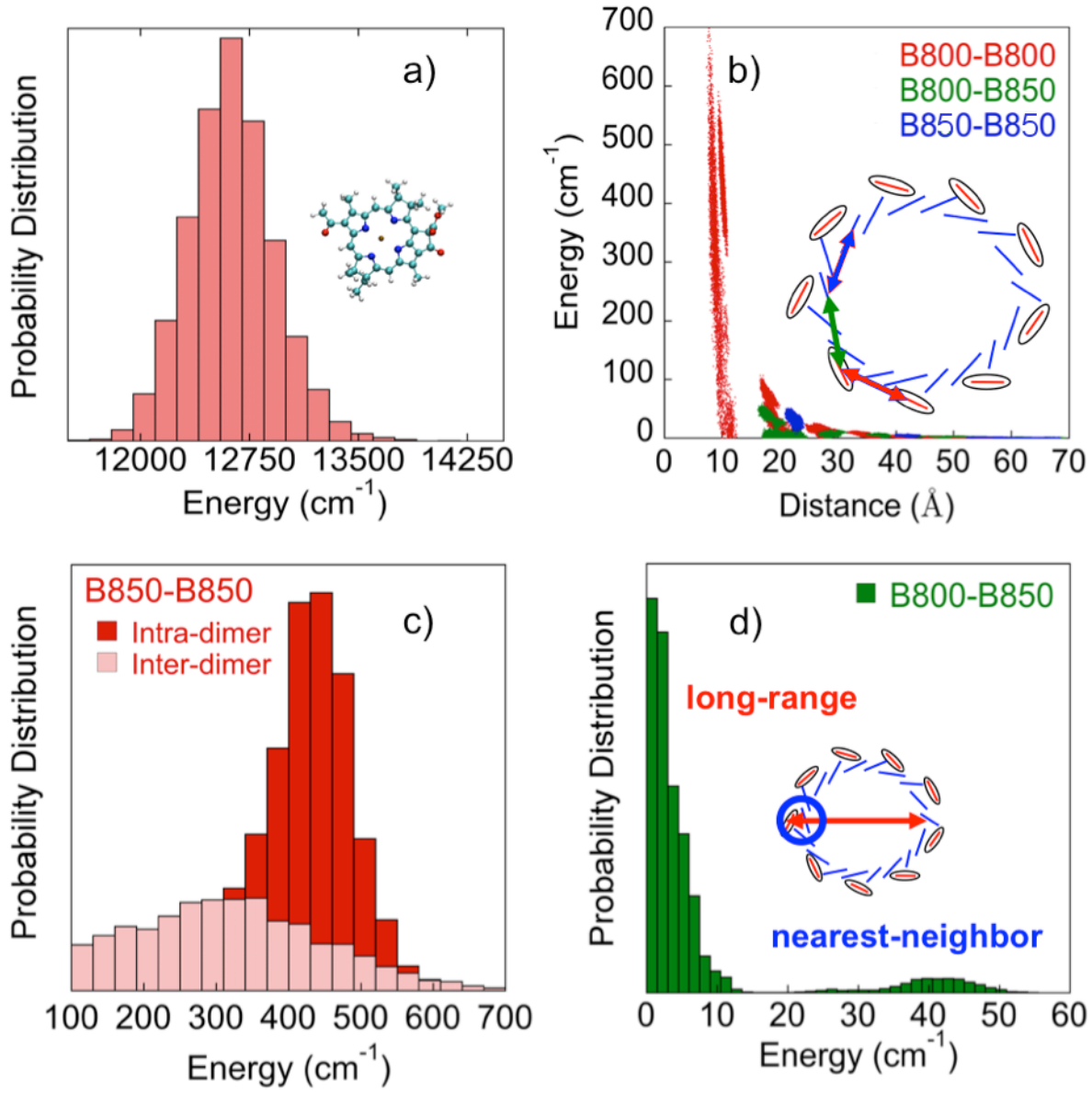

Figure 3: Distributions of exciton Hamiltonian matrix elements, computed from the same 500 trajectory snapshots and fitted parameters used to compute the absorption spectrum. The top two panels show (a) the distribution of vertical excitation site energies [$\varepsilon_{(i,k)} + \delta$ on the RHS of Eq. (3)] of each chromophore; (b) the distribution of off-diagonal matrix elements describing the intra-chromophore coupling within the B800 ring (blue), the B850 ring (red) and between chromophores in the B850 and B800 rings (green). The LH2 chromophores are represented as red and blue bars corresponding to the positions of B800 and B850 chromophores, respectively. The bottom two panels show (c) the distributions of nearest neighbor inter- (light red) and intra- (dark red) dimer coupling matrix elements, and (d) the distribution of coupling matrix elements between B800 and B850 chromophores.

4.2 Non-adiabatic exciton dynamics

Initial coordinates for the surface-hopping dynamics were determined by randomly choosing a single LH2 conformation from our ground state MD simulations, with initial velocities sampled from a 300K Boltzmann distribution. Our initial conditions, chosen to allow us to compare our results to the experiments recently reported by Maly et al.,[96] correspond to vertical Frank-Condon excitation by a Gaussian pulse centered at 800 nm (1.55 eV), corresponding to the B800 absorption band maximum. The pulse envelope was chosen to have a FWHM of 100 fs (~0.02 eV). The exciton eigenstates were initialized with total population normalized to unity according to Eq. (11). Time-dependent observable quantities, (e.g., those shown in Figure 4, discussed in further detail below) were computed from the population amplitudes propagated on each eigenstate via the single surface hopping trajectory.

Figure 4A shows the fluctuating excitonic eigenstate energies obtained in our single trajectory, and provides a time resolved picture of how dynamical disorder impacts the state energies within the eigenstate manifold. The color of the lines reflects the time-dependent Ehrenfest probability amplitudes calculated from solving Eq. (10), with more intense colors corresponding to a higher probability, less intense colors corresponding to a lower probability, and white corresponding to a zero probability. The dark red line shows the energy of the surface hopping trajectory as a function of time. Figure 4B shows the aggregate population in the 850 nm band over the first 300 fs of the surface hopping trajectory whose eigenstates are depicted in the top panel. The results over the first 300 fs indicate that the 850 nm band population created in the wake of the B800 excitation pulse grows with a time profile that is roughly exponential. Fitting the results in Figure 4B to an exponential growth kinetic model of the form

$$P_{B850}(t) = 1 - \exp(-t / \tau_{B800 \to B850}) \tag{14}$$

gives $\tau_{B800 \to B850} \sim 1050$ fs. The error in this fit is large owing to the fact that we have data from only a single non-adiabatic trajectory of limited (300fs) duration. The population growth curve is therefore noisy and fitted time constants longer than the trajectory duration will have considerable uncertainty. To get a better handle on the fitting error, we carried out an additional fit, to the envelope of the Fig 4B population trace. This gives $\tau_{B800 \to B850} \sim$ 650 fs. While more detailed comparison with experimental measurements will require longer time simulations and better statistics via sampling over a wider range of initial conditions (a topic for future work), the $\tau_{B800 \to B850}$ values obtained from

Figure 4B are nevertheless broadly in line with experimental measurements of the timescales for B800→B850 population transfer, which have been reported to range from 600 – 1000 fs.[89]

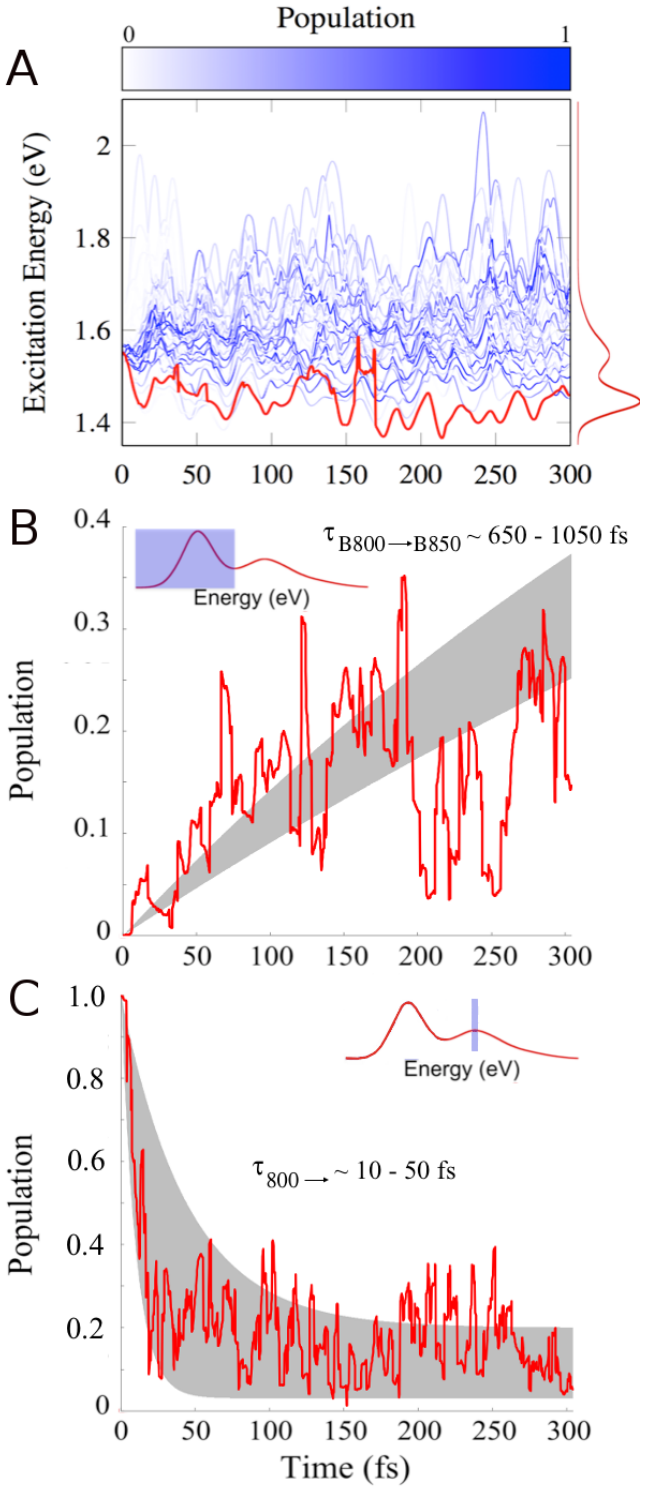

Figure 4: (A) Energies within the exitonic eigenstate manifold as a function of time. The intensity of each line corresponds to the population of the corresponding eigenstate at a particular time (white corresponds to zero population; dark blue to unit population).The energy of the surface-hopping trajectory as a function of time is depicted as a dark red line. The computed absorption spectrum is shown at the far right for reference, with the initial excitation and population distribution located at the 800 nm peak (1.55 eV). (B) Aggregated population summed over all eigenstates whose energy lies within the 850 band, using the shaded blue energetic range shown overlaid on the absorption spectrum in the inset. The grey region shows potential fits of the data to Eq (14). The fits are bounded by time constants of 650 and 1050 fs. (C) Aggregated population summed over all eigenstates whose energy lies within the 800 ± 5 nm band, using the shaded blue energetic range shown overlaid on the absorption spectrum in the inset. The grey region shows potential fits of the data to Eq (15). The fits are bounded by time constants of 10 and 50 fs.

Fig 4C shows the aggregated time-dependent population summed over all eigenstates whose energy lies within the 800 ± 5nm band, along with corresponding fits carried out using an exponential decay kinetic model of the form

$$P_{B800}(t) = [1 - P(\infty)] \cdot \exp(-t / \tau_{800\rightarrow}) + P(\infty) \quad (15)$$

Again, the data is noisy owing to the fact that we have only one trajectory; the grey bands show fits bounded by curves where $\tau_{800\rightarrow}$ ranges from 10 – 50 fs. Computing $\tau_{800\rightarrow}$ in this way allows us to undertake comparisons with recent work published by Maly et al,[96] who carried out pump-probe measurements of the distribution of ultrafast single-molecule relaxation times for LH2 in *Rhodopseudomonas acidophila*. By measuring the time-dependent population of initially excited excitonic states narrowly clustered around 800 nm, they obtained a distribution of relaxation times spanning 50 – 250 fs, with an average of 106 fs. Rather than being normally distributed, they specifically noted that their relaxation time distribution had a tail at longer times. The fitted values of $\tau_{800\rightarrow}$ obtained from the Figure 4C data are amongst the faster relaxation times reported by Maly et al., but nevertheless broadly in line with their measurements. By carrying out simulations over a wider range of initial conditions in future studies, it should be possible to directly calculate a distribution of $\tau_{800\rightarrow}$, like that reported by Maly et al.

4.3 Visualization of non-adiabatic LH2 exciton dynamics

The method outlined in this paper represents the first attempt to carry out atomistically-resolved on-the-fly *ab initio* non-adiabatic dynamics of LH2 exploiting recent developments in GPU-accelerated quantum chemistry and *ab initio* molecular dynamics. The parallel framework that we have outlined herein scales linearly with the number of excitonic basis functions, but nevertheless presents a significant computational expense. We are making progress in porting the framework outlined herein onto larger computational platforms, which will ultimately enable us to statistically converge the LH2 surface-hopping simulations and derive more quantitative conclusions related to excitonic energy transfer rates. However, even at this stage, we believe that the surface hopping dynamics allow us to draw important microscopic physical insight into the dynamics of excitonic energy transport which takes place in supramolecular biomolecular light-harvesting systems like LH2. In order to easily visualize the character of energy transport that we observe, we have constructed a movie showing time resolved excitonic energy transport in LH2 from our surface-

hopping dynamics (included as a movie link [see file NonAdiabaticDynamics.mov] in the Electronic Supplementary Information (ESI)).

Tools for constructing time-resolved depictions of excitonic energy transport are not generally available within standard molecular visualization packages. To construct the movie in the ESI, the 3D structural data (time-dependent atomic positions as a multi-state PDB file) were imported into Cinema 4D (http://www.maxon.net), a general-purpose modelling, animation, and rendering application. Import was achieved using ePMV (embedded Python Molecular Viewer), which allows the embedding of molecular modelling data into professional animation software environments to generate structures for visualization.[97] We represented the carbon backbones of the chromophores using stick models surrounding a central space-filling Mg atoms. We also utilized depth cuing, so that the opacity gradients of colours and lines used to represent the atomic stick models that make up the chromophores fade into the white background as they get deeper into the screen (i.e., with increasing Z-depth). In addition to the time series of atomic coordinates, the corresponding excitonic eigenstate amplitudes from the surface hopping simulations were projected onto the chromophore site-basis (i.e., by summing the population-weighted squares of the corresponding eigenvector coefficients) and imported into Cinema 4D (C4D) as a time series sequenced to the time-dependent atomic coordinate series. Excitonic amplitudes (within the site-basis representation) were represented as large spheres (each with an identical diameter), centred on the Mg atoms and coloured with a diffuse red. The centre of each exciton site-basis sphere has an opacity of 100%, and a soft edge which fades to 0% (i.e., full transparency). To enable direct visual comparison of the excitonic intensities within the site basis that makes up the LH2 excitonic eigenstates, we did not implement any depth queing of the excitonic clouds. Rather, we normalized the time-dependent amplitudes of the constituent excitonic site bases; this was accomplished through dividing all amplitudes by the maximally observed excitonic site basis amplitude. We wrote an embedded script within C4D to read the normalized amplitude of each excitonic site basis function, and subsequently modulate the opacity of each site-basis sphere at a specific timestep. Within the normalized amplitudes, a value of 1 corresponds to a sphere, which is 100% opaque, and a value of 0 corresponds to a sphere which is 100% transparent. The 300 fs of simulation (0.2 fs per timestep) was then used to construct a movie 1500 frames long that plays at 30 frames per second.

Section S3 of the ESI includes the Cinema 4D script which we used to generate the snapshots in Figure 5 (and the corresponding ESI movie), along with detailed instructions on how to use this script to read in time series of atomic coordinates and excitonic amplitudes. Rendering of a high-

quality movie is required to visualize the subtle opacity differences in the excitonic amplitudes. Since the C4D package is not commonly used within the chemical and biochemical molecular visualization communities, section S4 of the ESI includes files, instructions, and associated python scripts that illustrate how to generate an excitonic dynamics movie using the Chimera package.

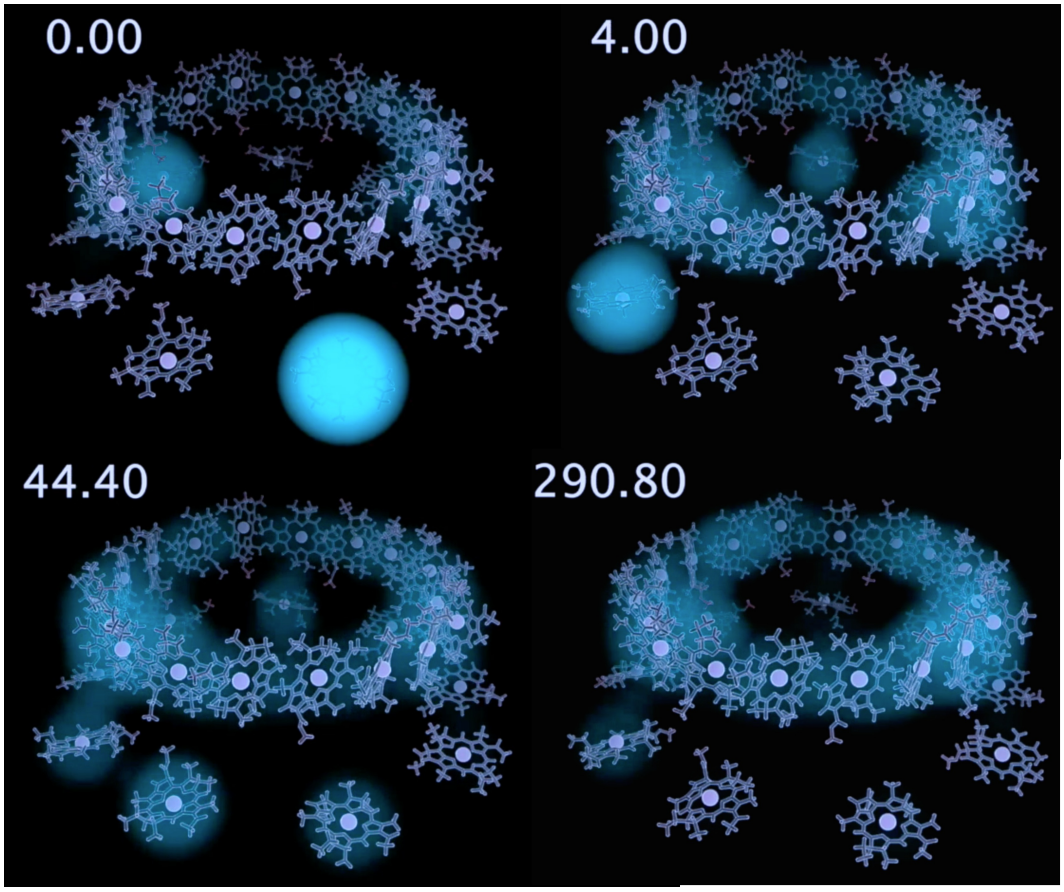

Figure 5: Snapshots from the supplementary movie, showing population amplitudes from surface-hopping trajectories projected into the chromophore site-basis as described in the text. The corresponding time (in fs) of each snapshot is also shown.

The picture of energy transport that emerges from the supplementary movie (excitonic state energies and populations used to make the movie are available in the LH2_population_data.zip folder included in the ESI) is that of extremely rapid transfer between delocalized excitonic eigenstates as a result of vibrational motion of the atoms that make up the constituent LH2 chromophores. This vibrational motion leads to frequent crossings in the excitonic eigenstate manifold, as shown in Figure 4. Figure 5 shows a select set of snapshots from the movie. At time zero, both Figure 5 and the accompanying supplementary movie show that the initial 800 nm excitation pulse places nearly all of the initial population in a localized state on the B800 ring. As time advances, electronic coupling between chromophores, modulated by vibronic fluctuations of the

constituent BChlas, drives hopping between rapidly fluctuating excitonic states, resulting in extremely rapid excitonic delocalization. Near the end of the 300 fs simulation window, the bottom panel of Figure 4 shows that the initial excitation has largely migrated to excitonic states on the B850 ring – a result which can also be seen from qualitative inspection of the 290.8 fs snapshot in Figure 5. The Supplementary Movie clearly shows that the timescale for excitonic transport is significantly faster than that for vibrational motion of the atoms that make up the chromophores.

5. Conclusions

In this work, we exploit a recently reported GPU-accelerated on-the-fly *ab initio* excitonic model[52] to carry out thousands of excited state *ab initio* calculations on the full LH2 complex in atomistic detail. This approach has allowed us to calculate a fully atomistic *in vacuo* absorption spectrum for LH2 which was calibrated using two parameters correcting for 1) intrinisic TDDFT errors in the monomer vertical excitation energies and 2) dielectric screening between monomers due to the surrounding protein environment that we have neglected. Optimization of these two parameters leads to an LH2 absorption spectrum that reproduces many of the features seen in the experimental spectrum – namely the double peak structure, the band edges, and the absorption linewidths. We expect our *ab initio* model to be quite accurate within the dynamically important regions of LH2 configuration space over which the model has been parameterized. We have further reported on the first fully atomistic *ab initio* calculations of nonadiabatic dynamics in LH2, using a surface hopping method for the dynamics. Future work will carry out the extensive averaging over initial conditions that is needed to make detailed predictions regarding excited state lifetimes and dynamical properties. It is important to point out that – for systems with stronger intermolecular interactions – the point dipole approximation utilized in this work may break down. As a result, one should exercise caution in extending the approach outlined herein to other systems, and carefully evaluate the goodness of the point dipole approximation for the specific system under investigation.

The results obtained from the on-the-fly surface hopping trajectory have allowed us to visualize the dynamics of excitonic migration in LH2. The data are noisy owing to the fact that we have only a single trajectory of limited duration (300fs); nevertheless we have been able to obtain approximate timescales, for B800 $\rightarrow$ B850 population transfer, as well as population relaxation of eigenstates centred at 800 nm. The results give values for $\tau_{B800 \rightarrow B850}$ between 650 – 1050 fs, and $\tau_{800 \rightarrow}$ between 10 – 50 fs, both of which consistent with published experimental observations. The dynamical picture of excitonic energy transport which emerges from this work is one of rapidly fluctuating excitonic eigenstates which are delocalized over multiple chromophores and undergo

frequent crossing on a femtosecond timescale as a result of the underlying vibrational dynamics of the atoms which make up the Bchla chromophores. The fluctuations of the Bchla vibronic bath result in disorder in both the Bchla site-energies (i.e., the diagonal elements of the exciton Hamiltonian) and also in the inter-chromophore couplings (i.e., the off-diagonal elements of the exciton Hamiltonian).

Nonadiabatic dynamics simulations for systems of this size provides an exciting challenge for even the most efficient TDDFT implementations, and requires additional levels of parallelism adapted to exploit modern supercomputing architectures. The results outlined in this work are therefore encouraging, but further work and computational resources are required in order to sample a more exhaustive range of initial conditions (including elliptically deformed LH2s), to converge the non-adiabatic dynamics statistics and improve the reliability of our predicted values of $\tau_{B800\to B850}$ and $\tau_{800\to}$. We also plan to explicitly treat the protein and solvent environment of the BChlas. With exascale parallel computational architectures on the horizon, it will become feasible to carry out atomistic nonadiabatic dynamics of separate LH2 complexes embedded in a membrane on timescales of tens of picoseconds, providing an unprecedented level of atomistic detail to understand and visualize light harvesting dynamics. We also intend to obtain other data from the model which will allow us to compare with experimentally measured circular dichroism spectroscopy, new types of 2d electronic-vibrational spectroscopy,[98] and LH2 superradiance predictions.[99] Ultimately, an atomistic framework such as this will allow us to go beyond mean-field treatments of the environment that use homogeneous, harmonic spectral densities. This will help determine the extent to which spatially heterogeneous atomic dynamics, nuclear vibrations, and local fluctuations of the chromophores/protein scaffold govern photosynthetic energy transport. Furthermore, it will furnish insight into the extent to which atomically resolved structural motifs and their dynamics modulate energy transfer.[46] Atomistic simulations along these lines will not only aid our attempts to visualize the relationship between energy transport and specific atomic motions, but also help to establish the appropriate dynamical phenomena for inclusion into less expensive coarse-grained models.

Acknowledgements

We thank Dr. Tom Oliver for a number of useful discussions. This work was supported by the AMOS program within the Chemical Sciences, Geosciences, and Biosciences Division of the Office of Basic Energy Sciences, Office of Science, U. S. Department of Energy under Contract No. DE-AC02-76SF00515. AS acknowledges funding from a DOE Computational Science Graduate Fellowship and a NSF Graduate Research Fellowship. TJM is a National Security Science and

Engineering Fellow (Office of the Assistant Secretary of Defense for Research and Engineering). DRG acknowledges funding as a Royal Society University Research Fellow, along with funding from EPSRC for MOC's PhD studentship. SMS acknowledges funding from the Royal Society, enabling him to undertake a research sabbatical at Stanford University. This project used the XStream computational resource supported by the NSF MRI program (ACI-1429830).

References

1. R. E. Blankenship, D. M. Tiede, J. Barber, G. W. Brudvig, G. Fleming, M. Ghirardi, M. Gunner, W. Junge, D. M. Kramer and A. Melis, *Science*, 2011, **332**, 805-809.
2. G. D. Scholes, G. R. Fleming, A. Olaya-Castro and R. van Grondelle, *Nat. Chem.*, 2011, **3**, 763-774.
3. R. Van Grondelle, *Biochim. Biophys. Acta*, 1985, **811**, 147-195.
4. E. Romero, R. Augulis, V. I. Novoderezhkin, M. Ferretti, J. Thieme, D. Zigmantas and R. van Grondelle, *Nat Phys*, 2014, **10**, 676-682.
5. R. J. Cogdell, A. Gall and J. Köhler, *Quart. Rev. Biophys.*, 2006, **39**, 227.
6. R. Kunz, K. Timpmann, J. Southall, R. J. Cogdell, A. Freiberg and J. Köhler, *Biophys. J.*, 2014, **106**, 2008-2016.
7. A. F. Fidler, V. P. Singh, P. D. Long, P. D. Dahlberg and G. S. Engel, *J. Chem. Phys.*, 2013, **139**, 155101.
8. A. F. Fidler, V. P. Singh, P. D. Long, P. D. Dahlberg and G. S. Engel, *J. Phys. Chem. Lett.*, 2013, **4**, 1404-1409.
9. E. E. Ostroumov, R. M. Mulvaney, J. M. Anna, R. J. Cogdell and G. D. Scholes, *J. Phys. Chem. B*, 2013, **117**, 11349-11362.
10. G. S. Schlau-Cohen, Q. Wang, J. Southall, R. J. Cogdell and W. E. Moerner, *Proc. Natl. Acad. Sci.*, 2013, **110**, 10899-10903.
11. R. Hildner, D. Brinks, J. B. Nieder, R. J. Cogdell and N. F. van Hulst, *Science*, 2013, **340**, 1448-1451.
12. R. van Grondelle and V. I. Novoderezhkin, *Physical Chemistry Chemical Physics*, 2006, **8**, 793-807.
13. M. Şener, J. Strümpfer, J. Hsin, D. Chandler, S. Scheuring, C. N. Hunter and K. Schulten, *ChemPhysChem*, 2011, **12**, 518-531.
14. M. Mohseni, P. Rebentrost, S. Lloyd and A. Aspuru-Guzik, *J. Chem. Phys.*, 2008, **129**, 174106.
15. T. C. Berkelbach, T. E. Markland and D. R. Reichman, *J. Chem. Phys.*, 2012, **136**, 084104.
16. T. Ritz, S. Park and K. Schulten, *J. Phys. Chem. B*, 2001, **105**, 8259-8267.

17. A. Damjanovic, I. Kosztin, U. Kleinekathöfer and K. Schulten, *Phys. Rev. E*, 2002, **65**, 031919.
18. S. Jang, E. Rivera and D. Montemayor, *J. Phys. Chem. Lett.*, 2015, **6**, 928-934.
19. S. Shim, P. Rebentrost, S. Valleau and A. Aspuru-Guzik, *Biophys. J.*, 2012, **102**, 649-660.
20. Y. Tanimura and R. Kubo, *J. Phys. Soc. Japan*, 1989, **58**, 101-114.
21. Y. Tanimura and R. Kubo, *J. Phys. Soc. Japan*, 1989, **58**, 1199-1206.
22. A. Ishizaki and G. R. Fleming, *J. Chem. Phys.*, 2009, **130**, 234111.
23. J. Strümpfer and K. Schulten, *J. Chem. Theory Comput.*, 2012, **8**, 2808-2816.
24. V. I. Novoderezhkin and R. van Grondelle, *Physical Chemistry Chemical Physics*, 2010, **12**, 7352-7365.
25. X. Hu, T. Ritz, A. Damjanovic and K. Schulten, *J. Phys. Chem. B*, 1997, **101**, 3854-3871.
26. T. Renger and F. Müh, *Phys. Chem. Chem. Phys.*, 2013, **15**, 3348.
27. J. Huh, S. K. Saikin, J. C. Brookes, S. Valleau, T. Fujita and A. Aspuru-Guzik, *J. Am. Chem. Soc.*, 2014, **136**, 2048-2057.
28. C. Stross, M. W. Van der Kamp, T. A. A. Oliver, J. N. Harvey, N. Linden and F. R. Manby, *The Journal of Physical Chemistry B*, 2016, **120**, 11449-11463.
29. D. Hayes, G. B. Griffin and G. S. Engel, *Science*, 2013, **340**, 1431-1434.
30. A. Halpin, P. J. M. Johnson and R. J. D. Miller, *Science*, 2014, **344**.
31. D. Hayes, G. B. Griffin and G. S. Engel, *Science*, 2014, **344**, 3.
32. A. W. Chin, J. Prior, R. Rosenbach, F. Caycedo-Soler, S. F. Huelga and M. B. Plenio, *Nature Phys.*, 2013, **9**, 113-118.
33. C. König and J. Neugebauer, *J. Chem. Theo. Comp.*, 2013, **9**, 1808-1820.
34. V. I. Novoderezhkin, E. Romero, J. Prior and R. van Grondelle, *Physical Chemistry Chemical Physics*, 2017, **19**, 5195-5208.
35. V. I. Novoderezhkin, E. Romero and R. van Grondelle, *Physical Chemistry Chemical Physics*, 2015, **17**, 30828-30841.
36. J. F. Galindo, E. Atas, A. Altan, D. G. Kuroda, S. Fernandez-Alberti, S. Tretiak, A. E. Roitberg and V. D. Kleiman, *J. Am. Chem. Soc.*, 2015, **137**, 11637-11644.
37. T. Mirkovic and G. D. Scholes, in *Photobiology: The Science of Light and Life*, ed. L. O. Björn, Springer New York, New York, NY, 2015, DOI: 10.1007/978-1-4939-1468-5_17, pp. 231-241.
38. R. Stones and A. Olaya-Castro, *Chem*, 2016, **1**, 822-824.

39. W. Domcke and D. R. Yarkony, *Ann. Rev. Phys. Chem.*, 2012, **63**, 325-352.
40. J. C. Tully, *J. Chem. Phys.*, 2012, **137**, 22A301.
41. B. G. Levine and T. J. Martinez, *Ann. Rev. Phys. Chem.*, 2007, **58**, 613-634.
42. T. J. Martinez and R. D. Levine, *J. Chem. Phys.*, 1996, **105**, 6334-6341.
43. T. J. Martinez, *Acc. Chem. Res.*, 2006, **39**, 119-126.
44. A. M. Virshup, C. Punwong, T. V. Pogorelov, B. A. Lindquist, C. Ko and T. J. Martinez, *J. Phys. Chem. B*, 2009, **113**, 3280-3291.
45. G. D. Scholes and G. Rumbles, *Nature Mat.*, 2006, **5**, 683-696.
46. G. D. Scholes and C. Smyth, *J. Chem. Phys.*, 2014, **140**, 110901.
47. A. L. Thompson, K. M. Gaab, J. Xu, C. J. Bardeen and T. J. Martinez, *J. Phys. Chem. A*, 2004, **108**, 671-682.
48. J. M. Herbert, X. Zhang, A. F. Morrison and J. Liu, *Acc. Chem. Res.*, 2016, **49**, 931-941.
49. N. H. List, C. Curutchet, S. Knecht, B. Mennucci and J. Kongsted, *J. Chem. Theo. Comp.*, 2013, **9**, 4928-4938.
50. J. J. Kranz and M. Elstner, *J. Chem. Theo. Comp.*, 2016, **12**, 4209-4221.
51. D. J. Cole, A. W. Chin, N. D. M. Hine, P. D. Haynes and M. C. Payne, *J. Phys. Chem. Lett.*, 2013, **4**, 4206-4212.
52. A. Sisto, D. R. Glowacki and T. J. Martínez, *Acc. Chem. Res.*, 2014, 140904081251004.
53. J. C. Tully, *J. Chem. Phys.*, 1990, **93**, 1061.
54. J. D. Jackson, *Classical electrodynamics*, Wiley, 1999.
55. C. Adamo and D. Jacquemin, *Chem. Soc. Rev.*, 2013, **42**, 845.
56. V. May and O. Kuhn, *Charge and Energy Transfer Dynamics in Molecular Systems*, Wiley-VCH, Weinheim, 2011.
57. G. D. Scholes, R. D. Harcourt and K. P. Ghiggino, *J. Chem. Phys.*, 1995, **102**, 9574.
58. M. Madjet, A. Abdurahman and T. Renger, *J. Phys. Chem. B*, 2006, **110**, 17268-17281.
59. B. P. Krueger, G. D. Scholes and G. R. Fleming, *J. Phys. Chem. B*, 1998, **102**, 5378-5386.
60. C. Weiss, *J. Mol. Spec.*, 1972, **44**, 37-80.
61. J. C. Chang, *J. Chem. Phys.*, 1977, **67**, 3901-3909.
62. K. J. Fujimoto, *J. Chem. Phys.*, 2012, **137**, 034101.
63. C. König, N. Schlüter and J. Neugebauer, *J. Chem. Phys.*, 2013, **138**, 034104.
64. J. Megow, T. Renger and V. May, *ChemPhysChem*, 2014, **15**, 478-485.
65. C. Steinmann and J. Kongsted, *J. Chem. Theo. Comp.*, 2015, **11**, 4283-4293.

66. J. Neugebauer, *The Journal of Physical Chemistry B*, 2008, **112**, 2207-2217.
67. A. F. Morrison and J. M. Herbert, *J. Phys. Chem. Lett.*, 2015, **6**, 4390-4396.
68. A. F. Morrison, Z.-Q. You and J. M. Herbert, *J. Chem. Theo. Comp.*, 2014, **10**, 5366-5376.
69. D. R. Glowacki, A. J. Orr-Ewing and J. N. Harvey, *J. Chem. Phys.*, 2011, **134**, 214508.
70. S. Coriani, T. Kjærgaard, P. Jørgensen, K. Ruud, J. Huh and R. Berger, *J. Chem. Theo. Comp.*, 2010, **6**, 1028-1047.
71. J. E. Subotnik, *J. Phys. Chem. A*, 2011, **115**, 12083-12096.
72. O. V. Prezhdo and P. J. Rossky, *J. Chem. Phys.*, 1997, **107**, 825.
73. E. R. Bittner and P. J. Rossky, *J. Chem. Phys.*, 1997, **107**, 8611-8618.
74. M. Ben-Nun and T. J. Martinez, *J. Chem. Phys.*, 1998, **108**, 7244-7257.
75. M. Ben-Nun and T. J. Martinez, *Adv. Chem. Phys.*, 2002, **121**, 439-511.
76. S. Yang and T. J. Martinez, in *Conical Intersections: Theory, Computation and Experiment*, eds. W. Domcke and H. Koppel, World Scientific, Singapore, 2011.
77. S. Hirata and M. Head-Gordon, *Chemical Physics Letters*, 1999, **314**, 291-299.
78. D. R. Glowacki, A. J. Orr-Ewing and J. N. Harvey, *J. Chem. Phys.*, 2015, **143**, 044120.
79. A. W. Götz, M. J. Williamson, D. Xu, D. Poole, S. Le Grand and R. C. Walker, *J. Chem. Theo. Comp.*, 2012, **8**, 1542-1555.
80. V. Cherezov, J. Clogston, M. Z. Papiz and M. Caffrey, *J. Mol. Biol.*, 2006, **357**, 1605-1618.
81. M. Ceccarelli, P. Procacci and M. Marchi, *J. Comp. Chem.*, 2003, **24**, 129-142.
82. L. Zhang, D.-A. Silva, Y. Yan and X. Huang, *J. Comp. Chem.*, 2012, **33**, 1969-1980.
83. K. N. Kirschner, A. B. Yongye, S. M. Tschampel, J. González-Outeiriño, C. R. Daniels, B. L. Foley and R. J. Woods, *J. Comp. Chem.*, 2008, **29**, 622-655.
84. A. Jakalian, D. B. Jack and C. I. Bayly, *J. Comp. Chem.*, 2002, **23**, 1623-1641.
85. A. Onufriev, D. Bashford and D. A. Case, *Proteins*, 2004, **55**, 383-394.
86. R. G. Alden, E. Johnson, V. Nagarajan, W. W. Parson, C. J. Law and R. G. Cogdell, *J. Phys. Chem. B*, 1997, **101**, 4667-4680.
87. J. Adolphs, F. Müh, M. E.-A. Madjet and T. Renger, *Photosyn. Res.*, 2008, **95**, 197-209.
88. G. D. Scholes, I. R. Gould, R. J. Cogdell and G. R. Fleming, *J. Phys. Chem. B*, 1999, **103**, 2543-2553.
89. G. D. Scholes and G. R. Fleming, *J. Phys. Chem. B*, 2000, **104**, 1854-1868.
90. M. Chachisvilis, O. Kühn, T. Pullerits and V. Sundstrom, *J. Phys. Chem. B*, 1997, **101**, 7275-7283.

91. R. Jimenez, S. N. Dikshit, S. E. Bradforth and G. R. Fleming, *J. Phys. Chem.*, 1996, **100**, 6825-6834.
92. M. H. C. Koolhaas, R. N. Frese, G. J. S. Fowler, T. S. Bibby, S. Georgakopoulou, G. van der Zwan, C. N. Hunter and R. van Grondelle, *Biochemistry*, 1998, **37**, 4693-4698.
93. G. Trinkunas and A. Freiberg, *J. Lumin.*, 2006, **119–120**, 105-110.
94. Y. Cheng and R. Silbey, *Phys. Rev. Lett.*, 2006, **96**, 028103.
95. M. Ketelaars, A. Van Oijen, M. Matsushita, J. Köhler, J. Schmidt and T. Aartsma, *Biophysical journal*, 2001, **80**, 1591-1603.
96. P. Malý, J. M. Gruber, R. J. Cogdell, T. Mančal and R. van Grondelle, *Proceedings of the National Academy of Sciences*, 2016, **113**, 2934-2939.
97. G. T. Johnson, L. Autin, D. S. Goodsell, M. F. Sanner and A. J. Olson, *Structure*, 2011, **19**, 293-303.
98. T. A. A. Oliver, N. H. C. Lewis and G. R. Fleming, *Proceedings of the National Academy of Sciences*, 2014, **111**, 10061-10066.
99. R. Monshouwer, M. Abrahamsson, F. van Mourik and R. van Grondelle, *The Journal of Physical Chemistry B*, 1997, **101**, 7241-7248.